

Visualizing orbital angular momentum induced single wavefront dislocation in graphene

Yi-Wen Liu^{1,*}, Yu-Chen Zhuang^{2,*}, Ya-Ning Ren^{1,*}, Chao Yan¹, Xiao-Feng Zhou¹, Qian Yang¹, Qing-Feng Sun^{2,3,†}, and Lin He^{1,‡}

¹Center for Advanced Quantum Studies, Department of Physics, Beijing Normal University, Beijing 100875, China, and Key Laboratory of Multiscale Spin Physics, Ministry of Education, Beijing 100875, China

²International Center for Quantum Materials, School of Physics, Peking University, Beijing 100871, China

³Hefei National Laboratory, Hefei 230088, China

*These authors contributed equally to this work.

†Correspondence and requests for materials should be addressed to Qing-Feng Sun (e-mail: sunqf@pku.edu.cn) and Lin He (e-mail: helin@bnu.edu.cn).

Phase singularities are phase-indeterminate points where wave amplitudes are zero, which manifest as phase vertices or wavefront dislocations. In the realm of optical and electron beams, the phase singularity has been extensively explored, demonstrating a profound connection to orbital angular momentum. Direct local imaging of the impact of orbital angular momentum on phase singularities at the nanoscale, however, remains a challenge and has yet to be achieved. Here, we study the role of orbital angular momentum in phase singularities in graphene, particularly at the atomic level, through scanning tunneling microscopy and spectroscopy. Our experiments demonstrate that the scatterings between different orbital angular momentum states, which are induced by local rotational symmetry-breaking potentials, can generate additional phase singularity, and result in robust single wavefront dislocation in real space. Our results pave the way for exploring the effects of orbital degree of freedom on quantum phases in quasiparticle interference processes.

Introduction

The phase of waves constitutes a fundamental parameter for all waves across diverse domains of physics^{1–9}. Phase singularity is an essential aspect of phase, denoting a phase indetermination point where the wave amplitude becomes zero. Encircling a phase singularity results in the accumulation of a certain phase, thereby initiating the emergence of additional wavefronts, i.e., additional surfaces of constant phase or wavefront dislocations in the wave field^{10–16}. In many cases, phase singularity is intimately related to orbital angular momentum. For instance, orbital angular momentum-carrying optical or electron beams usually exhibit spiral wavefronts, which involve phase singularities and further induce wavefront dislocations^{17–22}. These phenomena are widely observed through interference experiments on both macroscopic and microscopic scales, which have been extensively utilized in numerous applications^{17–27}.

However, it remains a challenge to explore the effects of orbital angular momentum on phase singularities at the nanoscale in condensed matter physics, owing to the limited available methods. Here, in two-dimensional (2D) massless Dirac fermions, we decipher the significance of orbital angular momentum effects by directly visualizing the wavefront dislocations in real space⁹. Specifically, by breaking the local rotational symmetry, inter-orbital angular momentum scatterings could occur, resulting in a transition of the interference pattern from two wavefront dislocations to a single one. The orbital angular momentum induced single wavefront dislocation is universally observed in rotationally asymmetric systems, regardless of whether the anisotropy originates from the potential of the tip or the geometry of the sample.

Phase singularity induced by inter-orbital angular momentum scatterings

Firstly, we briefly demonstrate the emergence of two wavefront dislocations in Friedel oscillations contributed by intervalley scatterings without inter-orbital angular momentum scatterings, a phenomenon also studied in previous experiments⁹. A process of intervalley scattering induced by the atomic defect or adatom in graphene is schematically shown in Fig. 1a. An incident wave from sublattice B in K valley, is scattered by the defect-induced local potential located at sublattice A, and then propagates back to the original position in K' valley. Since the local potential behaves like an isotropic hard wall, the intervalley scattering process hardly induce a change in the orbital angular momentum of electrons. Instead, due to the distinctive pseudospin textures for two valleys as shown in Fig. 1c, the intervalley scattering along intervalley scattering direction $\Delta\vec{K} = \vec{K} - \vec{K}'$ causes pseudospin vector in sublattice space rotating by an angle of $\theta_{pseudo} = -2\theta_q$ (here θ_q is the azimuth angle of the incident wave with momentum \vec{q}), which comes from the two-component wave function, and does not occur in scattering processes of the conventional two-dimensional electron gases (2DEG)^{9,28–32}. This pseudospin rotation related momentum \vec{q} will further affect the spatial interference pattern and induce wavefront dislocations in Friedel oscillations. To see this, we can do

Fourier-filtering by only picking out the elastic backscattering along $\pm\Delta\vec{K}$ corresponding to two peaks in Fast Fourier Transform (FFT), which are 30 degree rotated reciprocal lattice vectors relative to graphene^{33,34}. By selecting peaks at the specific frequency in FFT, we can obtain the local density of states (LDOS) modulation $\Delta\rho$ at this frequency through the inverse FFT. This LDOS modulation $\Delta\rho$ results from the quantum interference between the incident and the scattering wave, corresponding to $\lambda = \frac{2\pi}{\Delta K} \approx 3.7\text{\AA}$ periodic cosine wave in real space, which is shown in left part of Fig. 1a and Fig. 1d (the color is the amplitude of the wave, and each stripe reflects the phase of the cosine wave). Specially, the pseudospin rotation as shown in Fig. 1c will contribute an additional phase shift $2\theta_r$ into LDOS fluctuations as a topological phase singularity: $\Delta\rho_B(\Delta\vec{K}, \vec{r}) \propto \cos(\Delta\vec{K} \cdot \vec{r} + 2\theta_r)$ (see Supplementary Section 1 and refs.^{9,30}). Here θ_r is the real space polar angle of \vec{r} relative to the defect, and the phase $2\theta_r$ becomes singular at $\vec{r} = 0$, and this singularity is also associated with the defect position in real space, which will be discussed later.

Since the $\Delta\rho_B$ is a single-valued function and must return to the same value after encircling the singularity along a closed loop, the corresponding phase accumulation should be a quantized topological number $2\pi N$ (N is an integer), which can generate additional wavefronts in LDOS. In real space, after encircling the defect (singularity) with the STM tip, $2\theta_r$ accumulate $2 * 2\pi = 4\pi$ phase (θ_r changes from 0 to 2π for a circle). Therefore, two wavefront dislocations can emerge in $\Delta\rho_B(\Delta\vec{K}, \vec{r})$, as illustrated in Fig. S1. Furthermore, we can also consider a similar intervalley scattering process for LDOS modulation on sublattice A, which does not exhibit any phase singularity: $\Delta\rho_A(\Delta\vec{K}, \vec{r}) \propto \cos(\Delta\vec{K} \cdot \vec{r})$ (see Supplementary Section 1 and refs.^{9,30}). In Fig. 1d, we schematically show the total charge density modulation $\Delta\rho(\Delta\vec{K}, \vec{r}) = \Delta\rho_A(\Delta\vec{K}, \vec{r}) + \Delta\rho_B(\Delta\vec{K}, \vec{r})$ (see details in Supplementary Section 1). Clearly, the result exhibits double Y-shaped fringes which is well consistent with previous study⁹. Additionally, as the momentum \vec{q} circles the Dirac point along an anticlockwise-oriented contour, the pseudospin will rotate $2\pi\xi$ with $\xi = \pm 1$ for K and K' valley, which yields the topological number (winding number) $W = \xi$ as well as the Berry phase $\gamma = \xi\pi$ (see Supplementary Section 1). Since the geometric phase shift $2\theta_r$ in LDOS modulation is directly related to the pseudospin rotation angle $2\theta_q$, $N = 2$ additional wavefronts following $2\pi N = 4|\gamma|$ also strongly reflects the topology of Dirac cones⁹.

To investigate the role of orbital angular momentum in scattering processes and its impact on the interference in LDOS, we introduce an anisotropic potential that extends over a range surrounding the defect potential, exhibiting a directional dependence at the atomic scale. In this case, the conservation of orbital angular momentum in the scattering process is broken, leading to the occurrence of inter-orbital angular momentum scatterings. At this time, except for a relative phase

between A and B sublattice from the pseudospin-locking texture shown in the Figs. 1a,c, an additional term of $e^{im\theta_r}$ on both A and B sublattices related to orbital angular momentum m could also contribute (see definitions in Supplementary Section 2).

As an example, in Fig. 1b, one incident wave (K valley) with $m = 0$ orbital angular momentum (similar to a plane wave) is scattered by local anisotropic potential on sublattice A. It then returns as a reflected wave (K' valley) to the original position but possesses an orbital angular momentum $m = 1$, forming like a spiral wave. In particular, the incident wave has a constant phase structure, while the reflected wave possesses a helical phase structure represented by $e^{i\theta_r}$, as shown by the color in Fig. 1e. Therefore, the interference between the incident wave and reflected wave leads to the additional induction of a phase θ_r from orbital angular momentum difference. Now, both contributions from the pseudospin vector rotation and the interaction among orbital angular momentum states can shift the phase in LDOS modulation for B sublattice from $2\theta_r$ to $2\theta_r - \theta_r = \theta_r$ with $\Delta\rho_B(\Delta\vec{K}, \vec{r}) \propto \cos(\Delta\vec{K} \cdot \vec{r} + \theta_r)$ (see Supplementary Section 2). As the tip encircles the defect, an accumulation of 2π phase occurs, resulting in a change from two wavefront dislocations into a single wavefront dislocation, as depicted in Fig. 1f.

Observation of orbital angular momentum modulated phase singularity and single wavefront dislocation

To explore the above-mentioned inter-orbital angular momentum scattering effects on Friedel oscillations at the nanoscale, we performed a quasiparticle interference (QPI) experiment utilizing scanning tunneling microscopy (STM) and density-tuned scanning tunneling spectroscopy (STS). The device geometry is shown in the top panel of Fig. 2a. To obtain the hydrogen chemisorption defect-rich graphene samples³⁵, we either employ high-hydrogen growth graphene and subsequently transfer it onto hexagonal boron nitride (hBN) substrates^{36,37}, as shown in top panel of Fig. 2a, or apply tip pulses directly onto graphene/germanium (Ge) heterostructures (Extended Data Fig. 1). The lower panel of Fig. 2a illustrates the relationship between intervalley scattering processes in momentum space and the electron trajectory in real space in the STM experiment. Electrons with momentum \vec{q} can be injected towards the defect by the STM tip at the position \vec{r} relative to the defect. As shown in the panel, the polar angle θ_q is directly related to the polar angle θ_r of the tip in real space by $\theta_r = \theta_q + \pi$. Since the θ_r and θ_q are closely intertwined, the rotation of pseudospin vectors $2\theta_q$ in momentum space can naturally generate phase singularities $2\theta_r$ in real space and wavefront dislocations in LDOS map through the relation $\theta_r = \theta_q + \pi$ (Ref. ⁹), as shown in Fig. 1 and Fig. 2a.

In our experiment, the hydrogen chemisorption defect in graphene exhibits two distinct types of wavefront dislocations, as summarized in Fig. 2. Figures 2b and 2f show two representative topographic images. Both defects have three-fold rotational symmetry with the highest site localized

at the center of a carbon atom, exhibiting similar features as a single-atom absorption in graphene⁹. The atomic defects can generate strong intervalley scattering, characterized as a threefold $\sqrt{3}\times\sqrt{3}$ scattering pattern with respect to the graphene lattice, as shown in the STM topography (Figs. 2b,f). The signals of the intervalley scattering can be clearly observed also in their FFT images^{33,34}, which show six inner bright spots rotated by 30 degrees with respect to the outer Bragg peaks (Figs. 2c,g).

As introduced in Figs. 1a,c,d, the pseudospin vector rotation $2\theta_q$ induced by intervalley scattering leads to $2 * 2\pi$ phase accumulation when encircling the defect and, consequently, can generate two wavefront dislocations (2π phase induces one additional equiphase line, which corresponds to one wavefront dislocation)^{9,31,32}. To elucidate this point, we isolate the intervalley signals and employ an inverse FFT to acquire the wavefront dislocations in a specific direction in real space, as illustrated in Fig. 2d. The wavefront image contains two parts of information. One aspect concerns the amplitude of the wavefunction, and the other aspect relates to the phase. Two wavefront dislocations are observed around defect A due to the 4π phase accumulation, in line with previous studies^{9,31,32}. The 3.7 Å-wavelength LDOS modulations originate from the momentum transfer vector at the iso-energy contour between different valleys^{33,34}, which is in agreement with the calculation incorporating only a defect-induced delta potential^{9,31,32}, as depicted in Fig. 2e (see Supplementary Section 3-4 for further details). It is worth noting that the appearance of two wavefront dislocations is consistently observed in various substrates, temperatures and under distinct filter conditions (Extended Data Fig. 1). All these two wavefront dislocations are localized in the vicinity of the defect within the distance of approximately 15 wavelengths (Extended Data Fig. 1). This range qualitatively establishes the size of our focus in all conditions.

We also identify the well-defined single wavefront dislocation around the atomic defect by applying inverse FFT to the image with a size that is nearly identical, as shown in Fig. 2h (defect B). The robustness of the counted number of wavefront dislocations has been confirmed under various filter conditions (Extended Data Fig. 2), and similar characteristics are also observed in several other atomic defects utilizing the same tip (Extended Data Fig. 3). Obviously, the single wavefront dislocation observed in this study deviates from the expected dual wavefront dislocations and cannot be only explained by the mechanism of pseudospin-related phase accumulation in real space. To investigate the origin of the single wavefront dislocation, we conducted measurements of the spatial-resolved LDOS map and STS spectra for the representative atomic defect. Figure 2j displays the dI/dV spatial map of defect B with a single wavefront dislocation. The LDOS surrounding the defect exhibits an approximately elliptical distribution, characterized by lower LDOS intensity in the upper left region, which suggests the presence of asymmetry in the system. The STS point spectra in Fig. 2k presents peaks (red arrows) with approximately equidistant energy spacing of about 40 meV, which also shows asymmetric distribution around the defect at some energies. The origin of these peaks is attributed to the tip-induced quasibound states in graphene. Because of the different work functions between the tip and sample, the scanning probe can be regarded as a local top gate^{38–40}, generating a local potential to confine massless Dirac fermions in graphene. The range of the tip-induced potential at

the gate voltage of 9 V, estimated based on the energy spacing of quasibound states^{41–43}, is approximately 15 nm. This potential range is on the same order of magnitude as the intervalley scattering region around the defect, characterized as a threefold $\sqrt{3} \times \sqrt{3}$ scattering pattern, which can potentially generate strong influence on the scattering processes. The existence of tip-induced gating effect is further corroborated by the observation of the charging peak⁴⁴, as shown in Fig. 2k (black arrow). The STS measurements under high magnetic fields reveal more pronounced asymmetric features for both quasibound states and the charging peak (Extended Data Fig. 4g).

In contrast, the distribution of LDOS in real space exhibits relative uniformity across the defect region containing two wavefront dislocations, indicating the absence of a rotational symmetry-breaking in the system (Extended Data Figs. 4a-f). The source for the distinct potentials mostly arises from the different STM tips used in the measurements: one is a gold coated tungsten tip, introducing a finite electric field in graphene, and the other is a tungsten tip with the similar work function as graphene^{44–47}. Moreover, the stability of the single wavefront dislocation is preserved across different directions, as illustrated in Fig. 2l,m (Extended Data Figs. 5-6 for wavefront dislocations at various energies and back-gate voltages). Based on the above observations, the anisotropic potential is the dominant factor causing discrepancy in the inverse FFT. The presence of a single wavefront dislocation can be attributed to the combined contribution of asymmetric potential induced inter-orbital angular momentum scatterings and pseudospin effects, which supports the hypothesis in Fig. 1 and will be further clarified in subsequent discussions.

Theoretical analysis of orbital angular momentum induced phase singularity and single wavefront dislocation

To understand the emergence of single wavefront dislocation theoretically, we investigate the total LDOS modulation $\Delta\rho(\omega, \vec{r})$ generated by the intervalley scattering, which is measured in the experiment by including both the defect-induced local potential and a rotationally asymmetric potential $V(r, \theta_r)$ spreading in a range around the defect. $\Delta\rho(\omega, \vec{r})$ can be formally written as the imaginary part of the complex scalar field (also see Supplementary Section 2):

$$\begin{aligned}\Delta\rho(\omega, \vec{r}) &= \Delta\rho_A(\omega, \vec{r}) + \Delta\rho_B(\omega, \vec{r}) = -\frac{1}{\pi} \text{Im} \left\{ e^{i\Delta\vec{K} \cdot \vec{r}} [a(r, \theta_r) + b(r, \theta_r)e^{i2\theta_r}] \right\} \\ &= -\frac{1}{\pi} \text{Im} \left\{ e^{i\Delta\vec{K} \cdot \vec{r}} \sum_{\Delta m} [a(r, \Delta m)e^{i\Delta m\theta_r} + b(r, \Delta m)e^{i\Delta m\theta_r}e^{i2\theta_r}] \right\}, \quad (1)\end{aligned}$$

$a(r, \Delta m)$ and $b(r, \Delta m)$ can be related to the amplitude of the LDOS modulation for intervalley scattering on sublattice A and sublattice B ($\Delta\rho_A(\omega, \vec{r})$ and $\Delta\rho_B(\omega, \vec{r})$), respectively, with the transfer of the orbital angular momentum Δm . An additional term $e^{i2\theta_r}$ appears along with $b(r, \Delta m)$, which corresponds to the contribution of pseudospin vector rotation. Moreover, a finite Δm from the inter-orbital angular momentum scattering also introduces a phase $\Delta m\theta_r$ on both sublattice components.

The situation of the wavefront dislocation depends on the phase singularity of this complex scalar field. When the potential $V(r, \theta_r)$ exhibits rotational symmetry, Δm must be zero and the phase is $2\theta_r$ on the B sublattice, which induces two wavefront dislocations in $\Delta\rho(\omega, \vec{r})$ (Extended Data 7). Note that the contribution from sublattice A to the overall LDOS modulation primarily affects the shape and position of the wavefront dislocations (see details in Supplementary Section 1). When the potential $V(r, \theta_r)$ shows rotational asymmetry, the inter-orbital angular momentum scatterings occur, and some terms can shift the phase to θ_r rather than $2\theta_r$. Under an appropriate potential $V(r, \theta_r)$, the low order terms $a(r, \Delta m = 1)$ and $b(r, \Delta m = -1)$, both with phase θ_r , emerge as the dominant contributions near $\vec{r} = 0$. They roughly contribute to the LDOS modulation as $\cos(\Delta\vec{K} \cdot \vec{r} + \theta_r)$ and a single wavefront dislocation is exhibited, as shown in Fig. 1f. In principle, the other terms may also contribute to the LDOS modulation, but the phase singularity which they induce could highly rely on the specific distributions of $a(r, \Delta m)$ and $b(r, \Delta m)$, and the wavefront dislocation can be far away from the defect. Thus, in this situation, $\Delta\rho(\omega, \vec{r})$ should exhibit one robust additional dislocation near the defect.

We also performed the qualitatively calculated intervalley FFT-filtered $\Delta\rho(\omega, \vec{r})$. Besides a defect-induced delta potential, we also consider a Gaussian potential $-V_0 e^{-r^2/R^2}$, and directly add one spread angle-dependent step potential field $V_1(r, \theta_r)$ on it to break the rotation symmetry (Supplementary Sections 3-4)⁴⁸. In Fig. 2i, we show the numerically calculated $\Delta\rho(\omega, \vec{r})$ for 0.26 eV with $\Delta\vec{K} = \left(-\frac{4\pi}{3\sqrt{3}a_{cc}}, 0\right)$, where $\Delta\vec{K} = \vec{K} - \vec{K}'$ is the momentum difference between two nearest valleys in the intervalley scattering process, and $a_{cc} = 0.142$ nm is the length of carbon-carbon bond. Different from the result for the rotationally symmetric potential shown in Extended Data Fig. 7, only one wavefront dislocation is observed in the vicinity of the origin, and the orientation of this wavefront dislocation is still collinear to $\Delta\vec{K}$. It demonstrates that 2π rather than 4π phase is accumulated after a circulation around the defect, strongly suggesting that the phase θ_r becomes dominant in $\Delta\rho(\omega, \vec{r})$ because of the interplay between the orbital angular momentum and pseudospin texture. The main features in Fig. 2i are well consistent with the experimental results in Fig. 2h, indicating the validity of our previous theoretical analysis. Particularly, the single wavefront dislocation exhibits a degree of robustness. Given that the pseudospin textures related to Dirac cones shown in Fig. 1c and the rotationally asymmetric potential near the defect shown in Fig. 1b persist over a range of energies, the scenario depicted in Fig. 1e, and the single wavefront dislocation could also hold for several energies (see Extended Data Fig. 8). And considering the change of intervalley FFT-filtering direction only influences $\Delta\vec{K}$ but hardly changes the pseudospin vector rotation and inter-orbital angular momentum scattering induced by a spread potential, the phase singularity and the single wavefront dislocation in filtered LDOS modulation $\Delta\rho(\omega, \vec{r})$ should not change with the

intervalley filtering direction (see Extended Data Fig. 9 and also Supplementary Section 1) .

Wide existence of orbital angular momentum induced phase singularity and single wavefront dislocation

The effect of rotational symmetry-breaking on inter-orbital angular momentum scatterings, which leads to the single wavefront dislocation, is explicitly confirmed by introducing one-dimensional (1D) ripples to defect-rich graphene samples, as summarized in Fig. 3. Figure 3a exhibits a representative topographic image of 1D graphene ripples, showing a strained monolayer graphene with a periodicity of 15 nm⁴⁹. The 1D strained system exhibits a strong rotational symmetry-breaking, as observed in both its structure and LDOS (Extended Data Fig. 10). Here, a tungsten tip is utilized to capture the LDOS in distinct regions, revealing the presence of a flat band corresponding to the pseudo-Landau level, along with pseudomagnetic confinement states situated in between, which is consistent with the previous experiments^{49,50}.

In Fig. 3b, a prominent threefold scattering feature is observed for the defect (defect C), which is located within the periodically strained structure with confinement states. We employ FFT analysis to visualize the intervalley scattering in Fig. 3c. The resulting FFT yields six distinct inner peaks with pronounced asymmetric intensities, hinting that the presence of the asymmetric structure and potential in this system. Similarly, we perform inverse FFT for intervalley scattering signals to visualize the LDOS modulation in real space. The single wavefront dislocation around the defect is robust at various orientations, as depicted in Figs. 3d-f (Extended Data Fig. 10 for wavefront dislocations at different energies). The study reveals that the anisotropic substrate, along with its corresponding asymmetric electromagnetic potential, can also induce inter-orbital angular momentum scatterings. The orbital angular momentum-modulated phase singularity consequently results in the phase change from $2\theta_r$ to θ_r in real space. This substrate engineering provides a versatile platform for creating customized structures and potentials to manipulate intervalley scattering processes in future experiments.

Conclusions

In conclusion, our study uncovers the crucial role of orbital angular momentum in processes of Friedel oscillations. The breakdown of orbital angular momentum conservation and the occurrence of inter-orbital angular momentum scatterings lead to additional phase singularities and result in the transformation of double Y-shaped fringes into a single wavefront dislocation. Through our numerical simulations, we successfully capture the orbital-structured pseudospin and the anomalous single wavefront dislocation in real space. Our study presents an innovative approach to deciphering the orbital angular momentum effect by examining phase shifts and wavefront dislocations at the atomic scale. Looking ahead, the successful implementation of optical and electron beams with orbital angular momentum has demonstrated promising potential across various fields²¹. Our results on Dirac fermions with orbital angular momentum advances the understanding of phase singularities and wavefront dislocations in lower dimensions within condensed matter physics. The concept of the

inter-orbital angular momentum scatterings induced phase singularity can be extended to arrays or a larger scale, which may offer potential applications in nanodevices, electron-optical setups³⁸, novel microscopy techniques²³, and quantum communication systems^{20,21}.

References

1. Berry, M. V. Natural Focusing and Fine Structure of Light. *Proc. R. Soc. Lond. A* **392**, 45–57 (1984).
2. Berry, M. Making waves in physics. *Nature* **403**, 21–21 (2000).
3. Mawet, D., Riaud, P., Absil, O. & Surdej, J. Annular Groove Phase Mask Coronagraph. *Astrophys. J.* **633**, 1191–1200 (2005).
4. Zhang, Y., Tan, Y.-W., Stormer, H. L. & Kim, P. Experimental observation of the quantum Hall effect and Berry's phase in graphene. *Nature* **438**, 201–204 (2005).
5. Fushman, I. *et al.* Controlled Phase Shifts with a Single Quantum Dot. *Science* **320**, 769–772 (2008).
6. Shytov, A. V., Rudner, M. S. & Levitov, L. S. Klein Backscattering and Fabry–Pérot Interference in Graphene Heterojunctions. *Phys. Rev. Lett.* **101**, 156804 (2008).
7. Melde, K., Mark, A. G., Qiu, T. & Fischer, P. Holograms for acoustics. *Nature* **537**, 518–522 (2016).
8. Fereshte, G. *et al.* An on/off Berry phase switch in circular graphene resonators. *Science* **356**, 845 (2017).
9. Dutreix, C. *et al.* Measuring the Berry phase of graphene from wavefront dislocations in Friedel oscillations. *Nature* **574**, 219–222 (2019).
10. Berry, M. Geometry of phase and polarization singularities, illustrated by edge diffraction and the tides. *Geometry of phase and polarization singularities illustrated by edge diffraction and the tides, in Second International Conference on Singular Optics (Optical Vortices): Fundamentals and Applications* **4403**, 1–12 (2001).
11. Dutreix, C. & Delplace, P. Geometrical phase shift in Friedel oscillations. *Phys. Rev. B* **96**, 195207 (2017).
12. Nye, J. F. & Berry, M. V. Dislocations in wave trains. *Proc. R. Soc. Lond. A* **336**, 165–190 (1974).
13. Dutreix, C., Bellec, M., Delplace, P. & Mortessagne, F. Wavefront dislocations reveal the topology of quasi-1D photonic insulators. *Nat. Commun.* **12**, 3571 (2021).
14. Roumpos, G. *et al.* Single vortex–antivortex pair in an exciton-polariton condensate. *Nat. Phys.* **7**, 129–133 (2011).
15. Leonard, J. R. *et al.* Moiré pattern of interference dislocations in condensate of indirect excitons. *Nat. Commun.* **12**, 1175 (2021).
16. Matthews, M. R. *et al.* Vortices in a Bose-Einstein Condensate. *Phys. Rev. Lett.* **83**, 2498–2501 (1999).
17. Verbeeck, J., Tian, H. & Schattschneider, P. Production and application of electron vortex beams. *Nature* **467**, 301–304 (2010).
18. Wang, X. *et al.* Recent advances on optical vortex generation. *Nanophotonics* **7**, 1533–1556 (2018).
19. Forbes, A., de Oliveira, M. & Dennis, M. R. Structured light. *Nat. Photonics* **15**, 253–262 (2021).
20. Shen, Y. *et al.* Optical vortices 30 years on: OAM manipulation from topological charge to multiple singularities. *Light Sci. Appl.* **8**, 90 (2019).
21. Uchida, M. & Tonomura, A. Generation of electron beams carrying orbital angular momentum. *Nature* **464**, 737–739 (2010).

22. McMorran, B. J. *et al.* Electron Vortex Beams with High Quanta of Orbital Angular Momentum. *Science* **331**, 192–195 (2011).
23. Kalinin, S. V. *et al.* Machine learning in scanning transmission electron microscopy. *Nat. Rev. Methods Prim.* **2**, 1–28 (2022).
24. Ni, J. *et al.* Multidimensional phase singularities in nanophotonics. *Science* **374**, eabj0039 (2021).
25. Chen, W. *et al.* Time diffraction-free transverse orbital angular momentum beams. *Nat. Commun.* **13**, 4021 (2022).
26. Song, D. *et al.* Unveiling pseudospin and angular momentum in photonic graphene. *Nat. Commun.* **6**, 6272 (2015).
27. Allen, L., Beijersbergen, M. W., Spreeuw, R. J. C. & Woerdman, J. P. Orbital angular momentum of light and the transformation of Laguerre-Gaussian laser modes. *Phys. Rev. A* **45**, 8185–8189 (1992).
28. Park, C.-H. & Marzari, N. Berry phase and pseudospin winding number in bilayer graphene. *Phys. Rev. B* **84**, 205440 (2011).
29. Castro Neto, A. H., Guinea, F., Peres, N. M. R., Novoselov, K. S. & Geim, A. K. The electronic properties of graphene. *Rev. Mod. Phys.* **81**, 109–162 (2009).
30. Dutreix, C. & Katsnelson, M. I. Friedel oscillations at the surfaces of rhombohedral N-layer graphene. *Phys. Rev. B* **93**, 035413 (2016).
31. Zhang, Y., Su, Y. & He, L. Local Berry Phase Signatures of Bilayer Graphene in Intervalley Quantum Interference. *Phys. Rev. Lett.* **125**, 116804 (2020).
32. Zhang, Y., Su, Y. & He, L. Quantum Interferences of Pseudospin-Mediated Atomic-Scale Vortices in Monolayer Graphene. *Nano Lett.* **21**, 2526–2531 (2021).
33. Mallet, P. *et al.* Role of pseudospin in quasiparticle interferences in epitaxial graphene probed by high-resolution scanning tunneling microscopy. *Phys. Rev. B* **86**, 045444 (2012).
34. Brihuega, I. *et al.* Quasiparticle Chirality in Epitaxial Graphene Probed at the Nanometer Scale. *Phys. Rev. Lett.* **101**, 206802 (2008).
35. González-Herrero, H. *et al.* Atomic-scale control of graphene magnetism by using hydrogen atoms. *Science* **352**, 437–441 (2016).
36. Jia, P. *et al.* Programmable graphene nanobubbles with three-fold symmetric pseudo-magnetic fields. *Nat. Commun.* **10**, 3127 (2019).
37. Liu, Y.-W. *et al.* Tunable Lattice Reconstruction, Triangular Network of Chiral One-Dimensional States, and Bandwidth of Flat Bands in Magic Angle Twisted Bilayer Graphene. *Phys. Rev. Lett.* **125**, 236102 (2020).
38. Zhao, Y. *et al.* Creating and probing electron whispering-gallery modes in graphene. *Science* **348**, 672–675 (2015).
39. Freitag, N. M. *et al.* Large tunable valley splitting in edge-free graphene quantum dots on boron nitride. *Nat. Nanotechnol.* **13**, 392–397 (2018).
40. Liu, Y.-W., Hou, Z., Li, S.-Y., Sun, Q.-F. & He, L. Movable Valley Switch Driven by Berry Phase in

Bilayer-Graphene Resonators. *Phys. Rev. Lett.* **124**, 166801 (2020).

41. Gutiérrez, C., Brown, L., Kim, C.-J., Park, J. & Pasupathy, A. N. Klein tunnelling and electron trapping in nanometre-scale graphene quantum dots. *Nat. Phys.* **12**, 1069–1075 (2016).
42. Lee, J. *et al.* Imaging electrostatically confined Dirac fermions in graphene quantum dots. *Nat. Phys.* **12**, 1032–1036 (2016).
43. Ge, Z. *et al.* Giant orbital magnetic moments and paramagnetic shift in artificial relativistic atoms and molecules. *Nat. Nanotechnol.* **18**, 250–256 (2023).
44. Wyrick, J. *et al.* Tomography of a Probe Potential Using Atomic Sensors on Graphene. *ACS Nano* **10**, 10698–10705 (2016).
45. Liu, X. *et al.* Visualizing broken symmetry and topological defects in a quantum Hall ferromagnet. *Science* **375**, 321–326 (2022).
46. Farahi, G. *et al.* Broken symmetries and excitation spectra of interacting electrons in partially filled Landau levels. *Nat. Phys.* **19**, 1482–1488 (2023).
47. Jiang, Y. *et al.* Tuning a circular p–n junction in graphene from quantum confinement to optical guiding. *Nat. Nanotechnol.* **12**, 1045–1049 (2017).
48. Zhuang, Y.-C. & Sun, Q.-F. Wavefront dislocations in graphene systems revealed by transport measurement. *Phys. Rev. B* **107**, 235423 (2023).
49. Ren, Y.-N., Zhuang, Y.-C., Sun, Q.-F. & He, L. Magnetic-Field-Tunable Valley-Contrasting Pseudomagnetic Confinement in Graphene. *Phys. Rev. Lett.* **129**, 076802 (2022).
50. Mao, J. *et al.* Evidence of flat bands and correlated states in buckled graphene superlattices. *Nature* **584**, 215–220 (2020).
51. Setvín, M. *et al.* Ultrasharp tungsten tips—characterization and nondestructive cleaning. *Ultramicroscopy* **113**, 152–157 (2012).
52. Lucier, A.-S., Mortensen, H., Sun, Y. & Grütter, P. Determination of the atomic structure of scanning probe microscopy tungsten tips by field ion microscopy. *Phys. Rev. B* **72**, 235420 (2005).

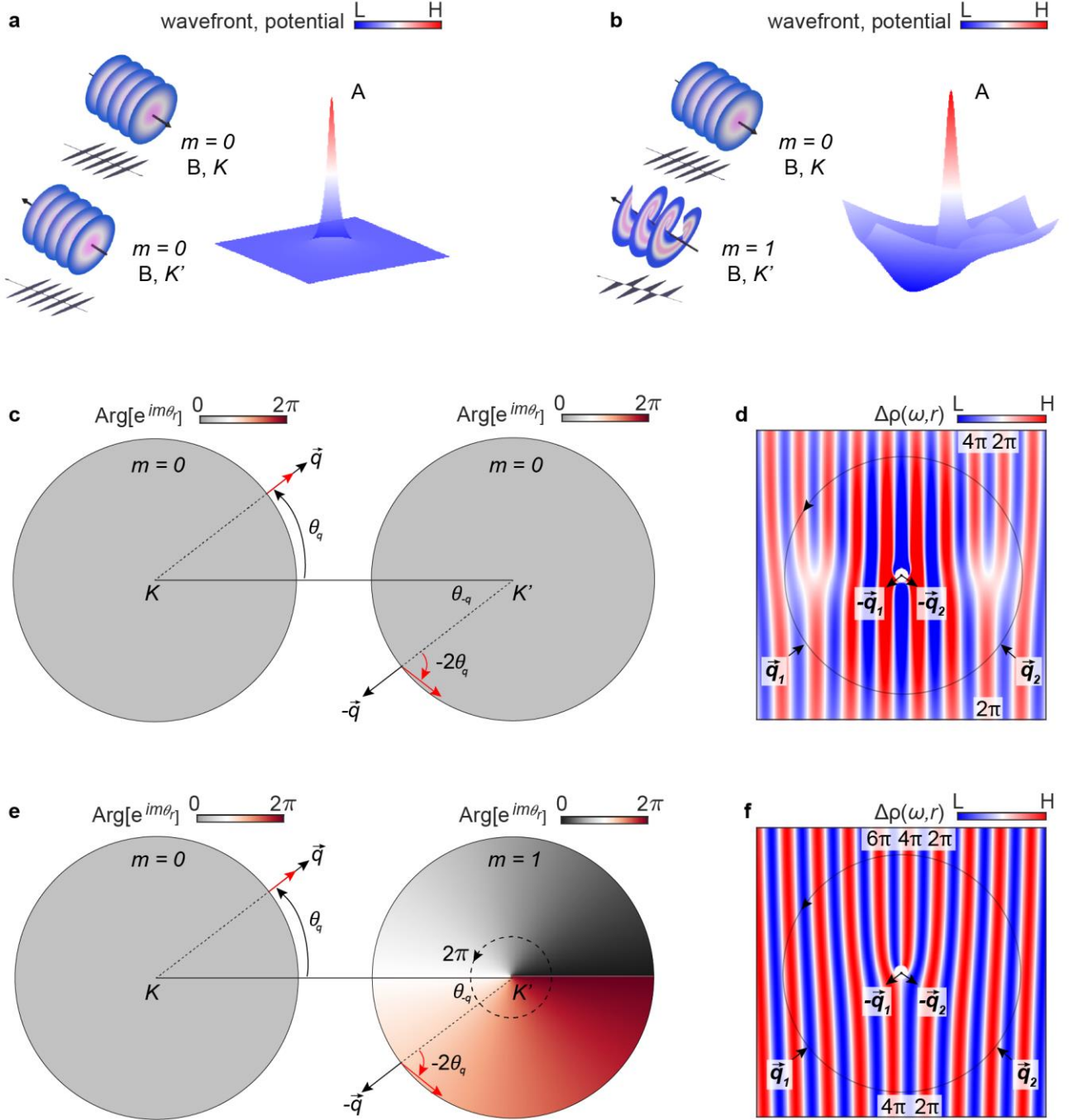


Fig.1 | Dynamics of intervalley scattering and wavefront dislocations. **a**, A schematic diagram of intervalley interference between the incident wave and the reflected wave due to the presence of a defect potential. The color scale represents the intensity distributions for both wavefronts and the potential. **b**, A wave scattering by a defect potential accompanied by a spread rotationally asymmetric potential, leading to reflection as a spiral wavefront with a finite orbital angular momentum. **c**, Intervalley scattering process for panel **a** between two nearest valleys, involving pseudospin rotation. Black and red arrows denote the vector of momentum \vec{q} and pseudospin, respectively. The color gradient from black to red represents the variation of the phase. **d**, A schematic diagram to show

detected by the tungsten tip (defect A, sample bias $V_b = 0.45$ V). Image size: 7×7 nm². **c**, FFT image of the defect A, and six inner peaks come from the intervalley scattering process. Right lower inset, a_1 , a_2 , and a_3 directions, which are defined according to the direction of intervalley scattering in FFT, are labelled. **d**, Experimental wavefront dislocations, which is extracted by filtering the red circles in panel **c**. Both $\pm\Delta\vec{k}$ are considered during the filtering. The splitting of the wavefront dislocations is due to the contribution from both A and B sublattices. **e**, Theoretical LDOS modulation in real space (energy: 0.44 eV). **f**, Experimental STM topography for another hydrogen chemisorption defect obtained via Au-coated tip (defect B, sample bias $V_b = 0.2$ V). Image size: 6×6 nm². **g**, FFT image of the defect in panel **f**. **h,i**, Experimental (energy: 0.21 eV) and theoretical (energy: 0.26 eV) wavefront dislocations, which are similar to those in panel **d,e**, with only one wavefront dislocation in inversed FFT images. **j**, dI/dV map obtained at $V_b = 0.2$ V, which shows asymmetric potential in real space. Image size: 6.7×6.7 nm². **k**, Derivative STS point spectra collected along the black line direction in panel **j** with a longer distance of about 20 nm, showing quasibound states (red arrows) and a charging peak (black arrow). **l,m**, Robust single wavefront dislocation in the other two directions (a_2 and a_3). Panels **f-m** are obtained at the same defect. The wavelength of wavefront dislocation is 3.7 Å.

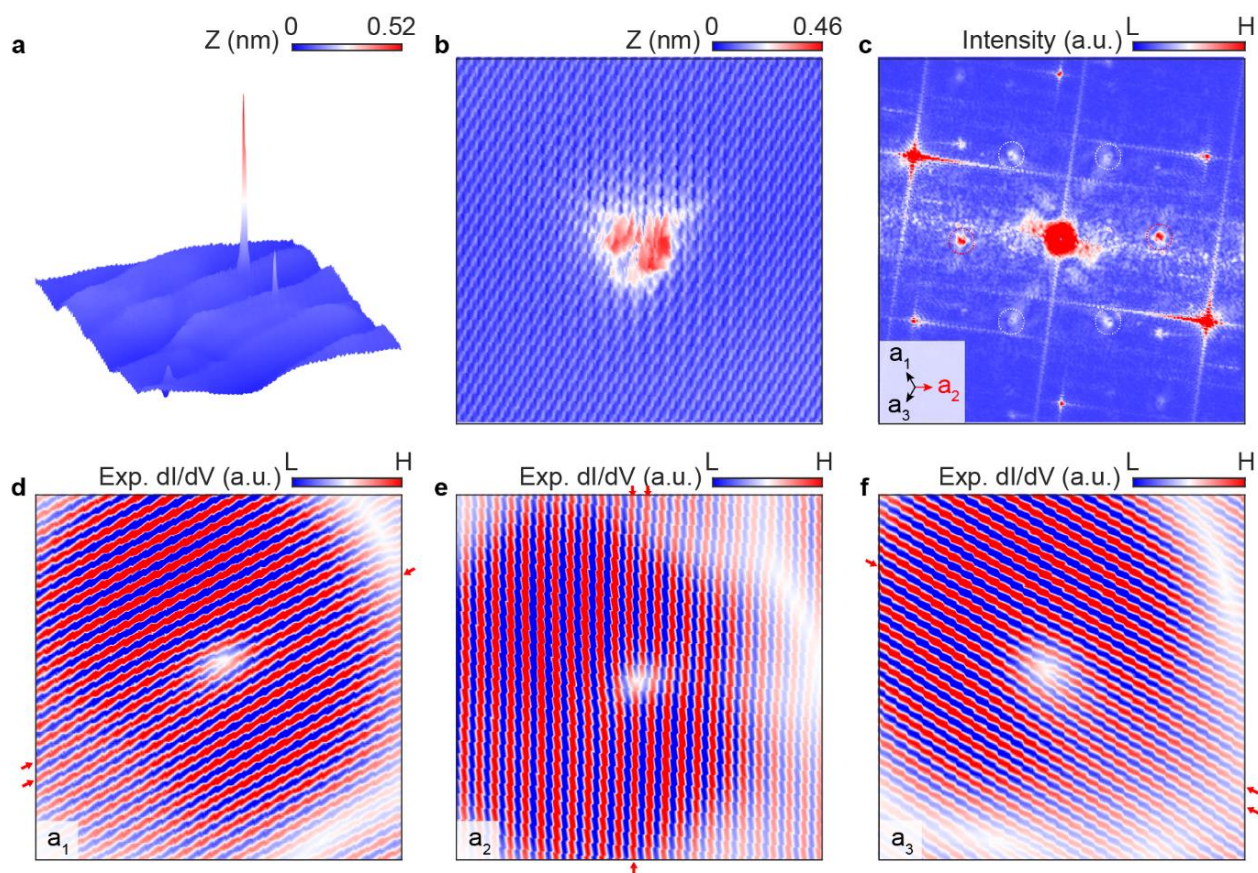


Fig.3| Single wavefront dislocation induced by anisotropic potential. **a**, STM geometry of the periodic strained graphene with a defect on it. The size of the scanning window is $70 \times 70 \text{ nm}^2$. **b**, An enlarged topographic image of a defect obtained through the tungsten tip (defect C, sample bias $V_b = 0.4 \text{ V}$) on the strained structure. Size of image: $8.3 \times 8.3 \text{ nm}^2$. **c**, FFT image of the defect in panel **b**. The inner asymmetric points result from intervalley scattering processes. The directions of intervalley scattering are marked in the inset with a_1 , a_2 , and a_3 . Size of image: $10.5 \times 10.5 \text{ nm}^2$. **d-f**, Experimental wavefront dislocations in real space which are filtered along a_1 , a_2 , and a_3 directions, which is perpendicular to the intervalley scattering peaks in panel **c**. The wavelength is about 3.7 \AA in these three interference images.

Methods

Sample fabrication

To obtain graphene samples with a high number of hydrogen chemisorption defects, we utilized two methods to intentionally introduce these defects. In the first method, we fabricated graphene samples using low-pressure chemical vapor deposition (LPCVD). We introduce hydrogen defects by adjusting the hydrogen ratio during the growth process. Subsequently, we transferred graphene to hBN substrates to investigate gate-dependent states in the vicinity of the defects. The contacts were made by evaporating Ti/Au (3 nm/30 nm). The samples were annealed at 300 °C in LPCVD and ultra-high vacuum before the STM measurements. The second approach involves directly creating graphene defects through the STM tip pulses on the Ge substrate. This method relies on the relatively low Ge-H bond energy and the desorption of hydrogen atoms facilitated by the pulse stimulation.

STM/STS measurements

STM and STS measurements were performed with commercial STM systems from UNISOKU (USM-1300/1400/1500) in an ultrahigh vacuum chamber with a pressure of about 10^{-11} Torr. The topography images were taken by turning on the feedback circuit. The dI/dV spectra were taken with a standard lock-in technique by turning off the feedback circuit and using a 793 Hz, 1-5 mV_{pp} modulation added to V_b with the time constant of 3-30 ms. d^2I/dV^2 was obtained through numerical differentiation. The STM tips were obtained by etching tungsten wires, and they were cleaned by e-beam heating before the measurements. The work functions of graphene sample and STM tips vary between 4.5-4.7 eV for graphene, 3.6-4.0 eV for gold-coated tips, and 4.86 eV for Pt-Ir tips⁴⁷, 4.5 eV for tungsten tips^{51,52}, respectively. The experimental results shown in the main text were all taken at around 4.2 K.

Data availability

The data that support the findings of this study are available from the corresponding author upon reasonable request.

Code availability

The code that supports the findings of this study is available from the corresponding author upon reasonable request.

Acknowledgements

We thank H. Zhou, Z. Zhan, Y. Su, W. Zhi, and P. Wu for discussions. This work was supported by the National Key R and D Program of China (Grants No. 2021YFA1401900 and No. 2021YFA1400100), the National Natural Science Foundation of China (Grants No. 12141401, No. 11974050, No. 12374034,

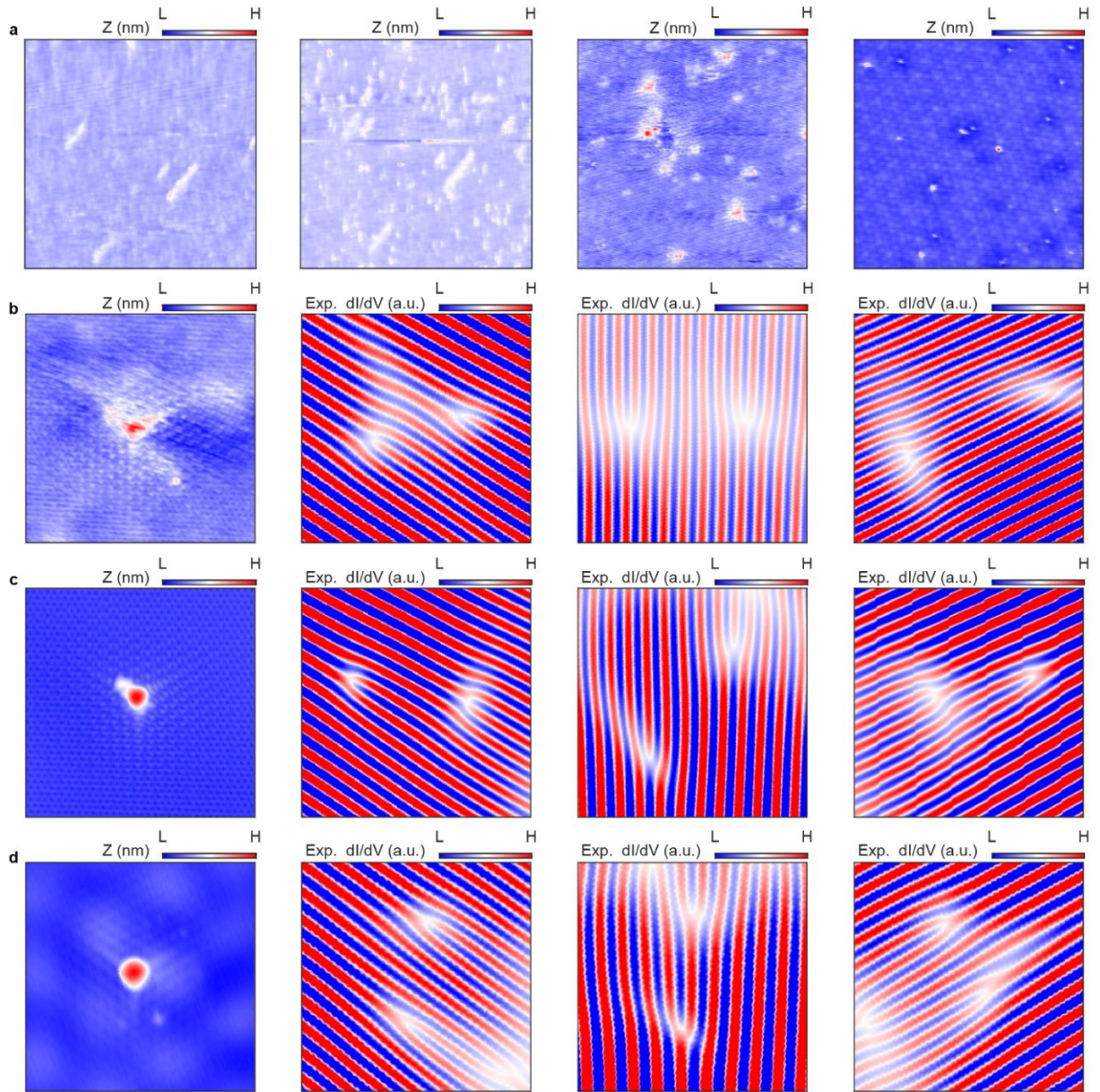
and No. 11921005), the Innovation Program for Quantum Science and Technology (2021ZD0302403), and the Strategic priority Research Program of Chinese Academy of Sciences (Grant No. XDB28000000), the Fundamental Research Funds for the Central Universities and the China Postdoctoral Science Foundation (2023M740296). The devices were fabricated using the transfer platform from Shanghai Onway Technology Co., Ltd.

Author contributions

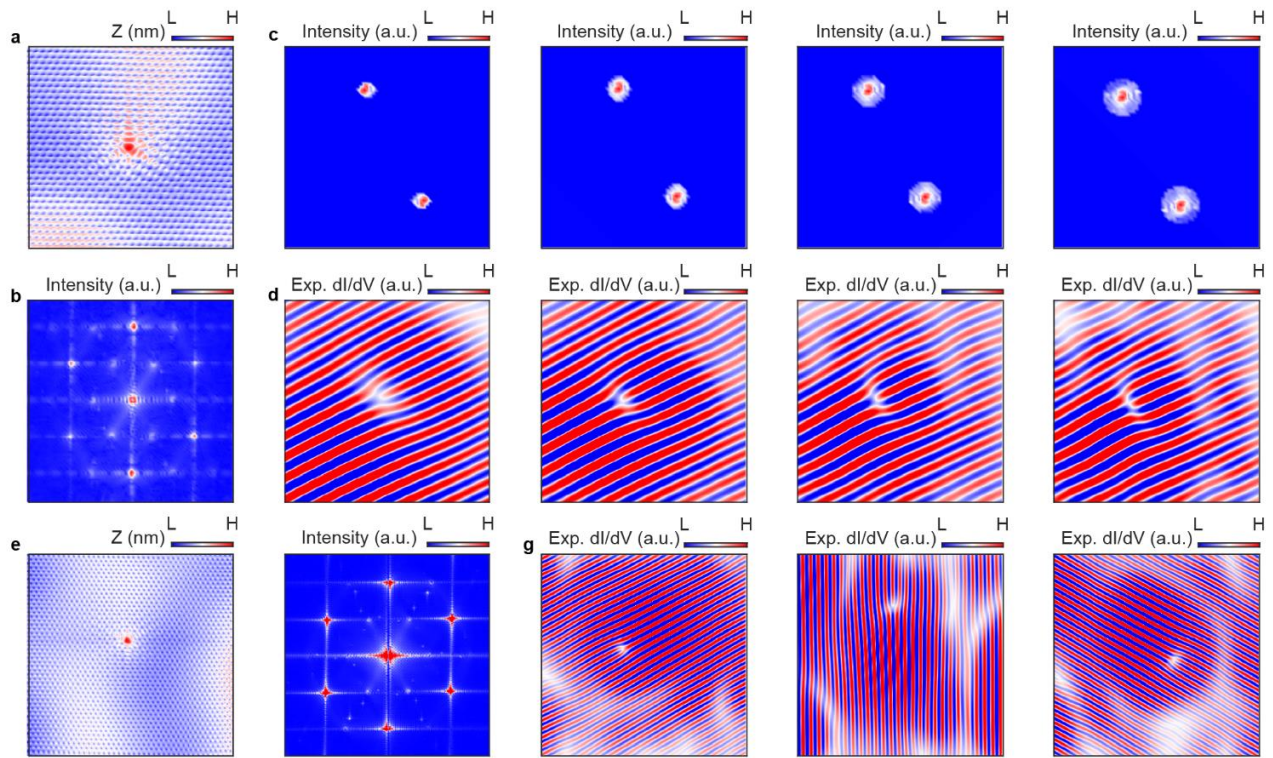
Y.L. and L.H. conceived the work and designed the research strategy. Y.L. fabricated the samples and carried out the STM and STS measurements. Y.R., C.Y., X.Z., and Q.Y. participated in the measurements and provided experimental data. Y.L. and Y.Z. performed the data analysis under the supervision of L.H. and Q.S. Y.Z. carried out the theoretical analysis and Green's function calculations under the supervision of Q.S. Y.L. and Y.Z. wrote the paper with input from L.H. and Q.S.

Competing financial interests

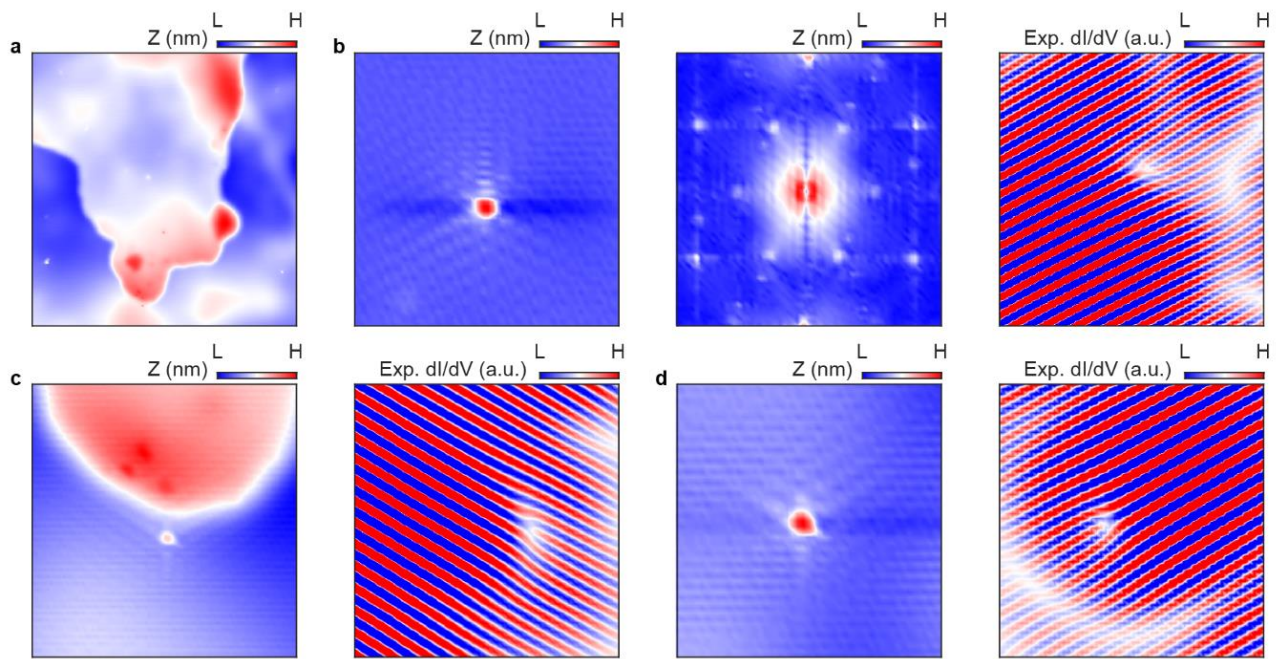
The authors declare no competing financial interests.



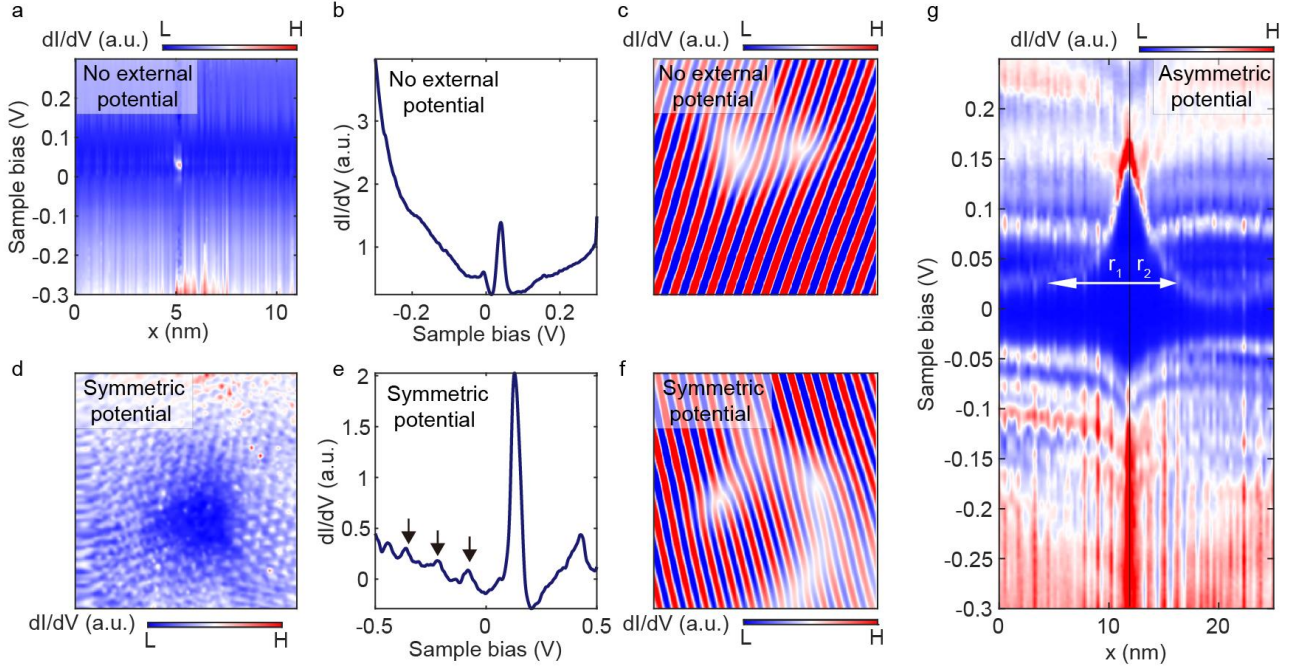
Extended Data Fig. 1 | Sample preparation and two wavefront dislocations in three directions. a, Generating Defects. From left to right: typical images of graphene on Ge substrate before and after STM tip pulses, zoom-in image of defects on Ge substrate, and defect-rich graphene on Cu substrate. **b, Defects on the semiconducting substrate.** The graphene defect and wavefront dislocations on Ge substrate. The defect is generated by the strong STM tip pulse around -4 V to 4 V. The tip pulse cuts off the Ge-H bond and creates hydrogen absorption underneath the monolayer graphene. **c, Defects on the insulating substrate.** Graphene defect and wavefront dislocations on BN substrate. The defect arises intrinsically during the growth process, and defect-rich graphene is subsequently transferred onto the BN substrate for gate-tunable measurements. **d, Defects on the metallic substrate.** One graphene defect on Cu-Ni substrate. The double wavefront dislocations are observed in three directions as well. The panels from **b** to **d** demonstrate the robust and universal nature of the wavefront dislocations across various systems.



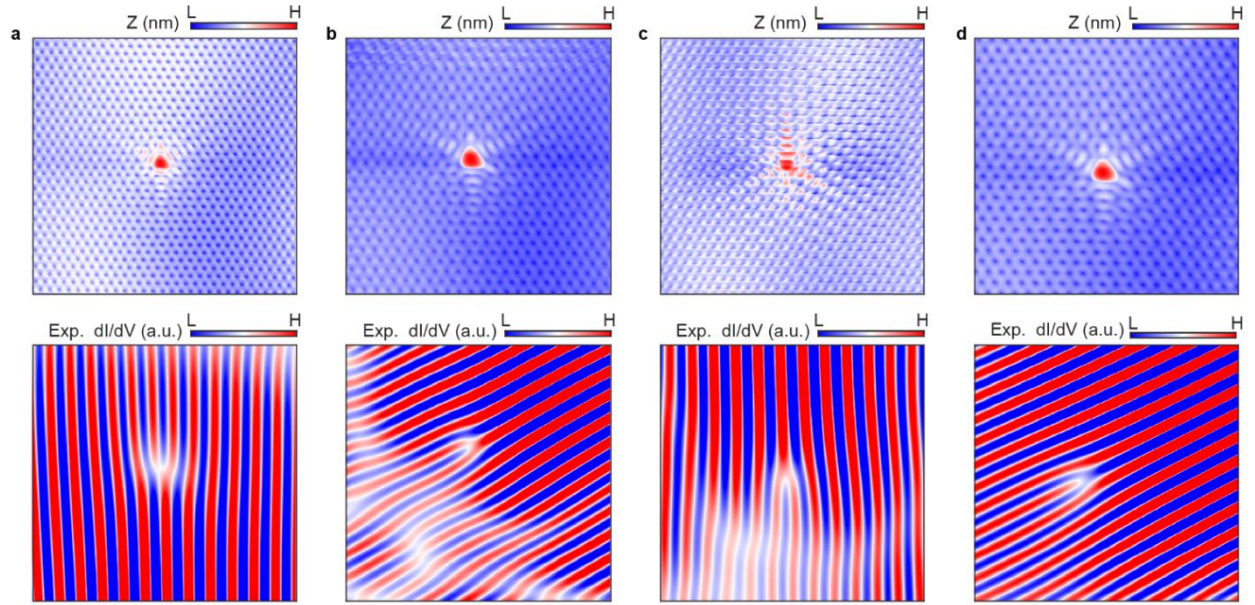
Extended Data Fig. 2 | Different filter conditions. **a-b**, One defect and the corresponding FFT image. Image size: $8 \text{ nm} \times 8 \text{ nm}^2$, sample bias $V_b = 0.6 \text{ V}$, setpoint $I = 0.3 \text{ A}$. **c-d**, Upper images display filtered circles of varying sizes, while the lower images represent the corresponding wavefront dislocations, which result from the inverse FFT of the upper images. There is always one wavefront dislocation with different filter sizes, which means the single wavefront dislocation is robust and not related to the filter conditions. **e-g**, A defect of the same type as above, but with a larger image size. The figures display topography, FFT, and wavefront dislocations in three directions from left to right, which illustrate that the single wavefront dislocation is still clean and robust in a larger window.



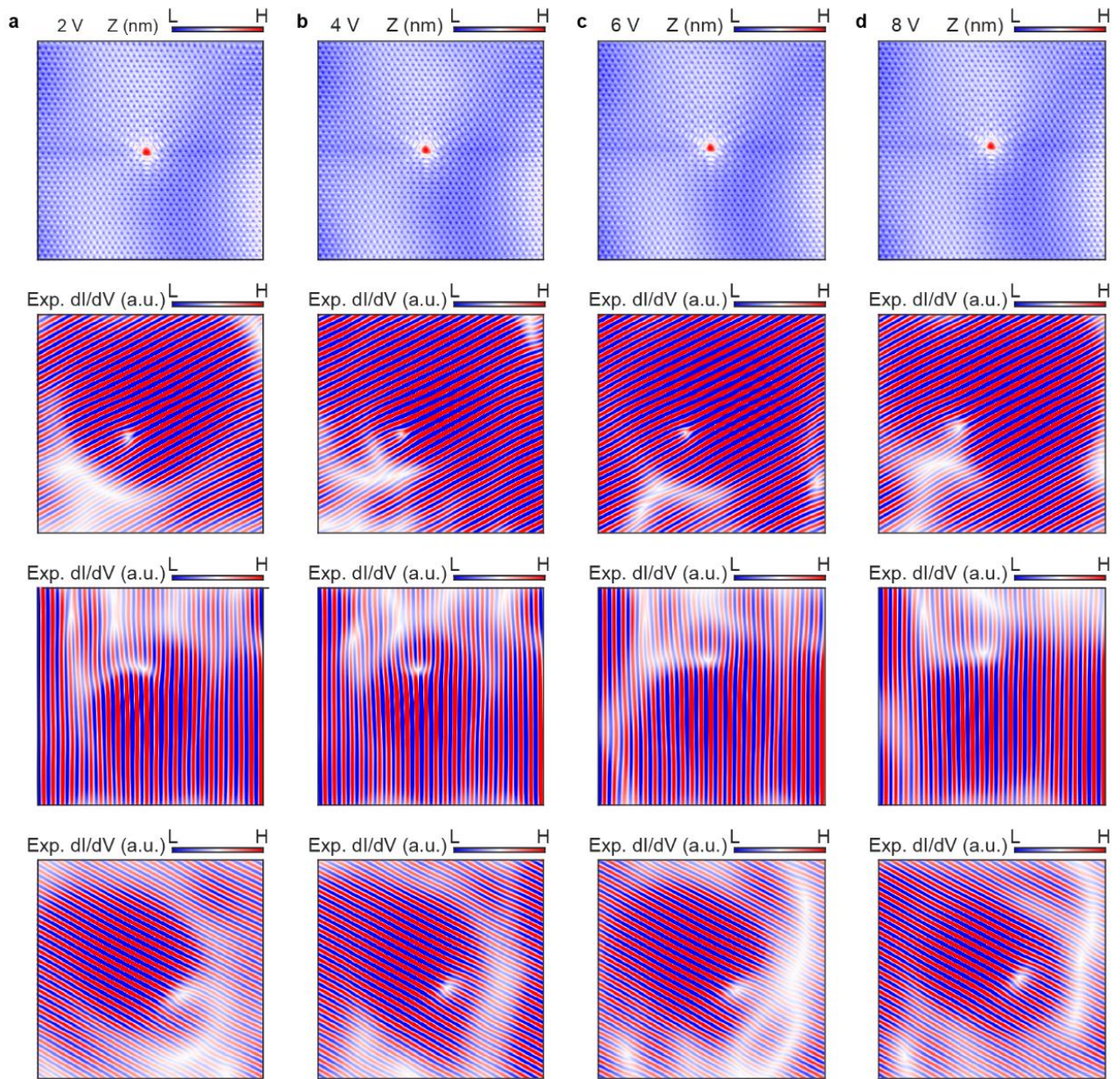
Extended Data Fig. 3 | Different defects detected by the same STM tip. a, Large area graphene-hBN topography with defects on it. **b-d,** Defects located on and off the step, along with their respective single wavefront dislocation. The presence of the same single wavefront dislocation across defects located in different areas indicates that this phenomenon is not caused by local interference from the substrate.



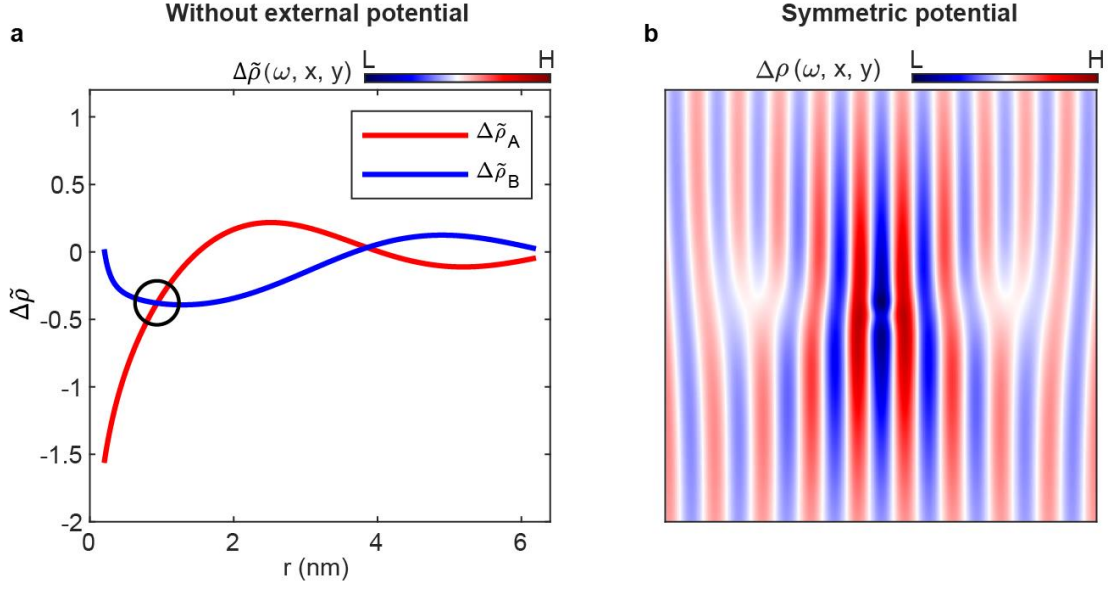
Extended Data Fig. 4 | Comparison of different types of potential. **a**, STS linecut obtained along a hydrogen chemisorption defect without external potential. The defect state, which shows high dI/dV intensity, is located at the same energy with the Dirac point of graphene. **b**, STS point spectra extracted from panel **a** around the defect. Only the defect state is observed in the STS. **c**, wavefront dislocations of the same defect as panel **a**, showing two wavefront dislocations in real space. **d-f**, STS map, STS point spectra, and two wavefront dislocations for another hydrogen chemisorption defect. STS map size: $6 \text{ nm} \times 6 \text{ nm}^2$. The LDOS in real space exhibits equal intensity surrounding the defect, indicating a relatively symmetric potential in comparison to Fig. 2f. Black arrows in panel **e** with uniform spacing denote the presence of a tip-induced quantum dot effect when detected in the vicinity of the defect region. **g**, STS linecut for the same defect as Fig. 2d under the magnetic field of 8 T. The charging peak shows the asymmetric distance for the same chemical potential, which can reflect the asymmetric tip potential.



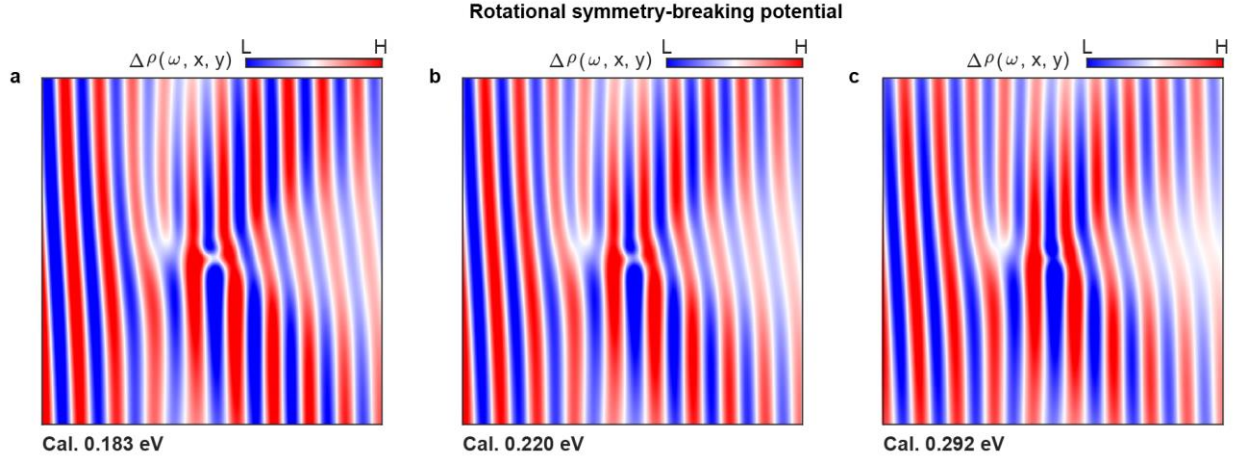
Extended Data Fig. 5 | Wavefront dislocations at distinct energies. a-d, Topographic images with different sample bias and setpoint, which are 0.3 V, 0.1 A; 0.5 V, 0.2 A; 0.6 V, 0.3 A; 0.7 V, 0.2 A. The wavefront dislocations at the bottom are derived from the upper defects.



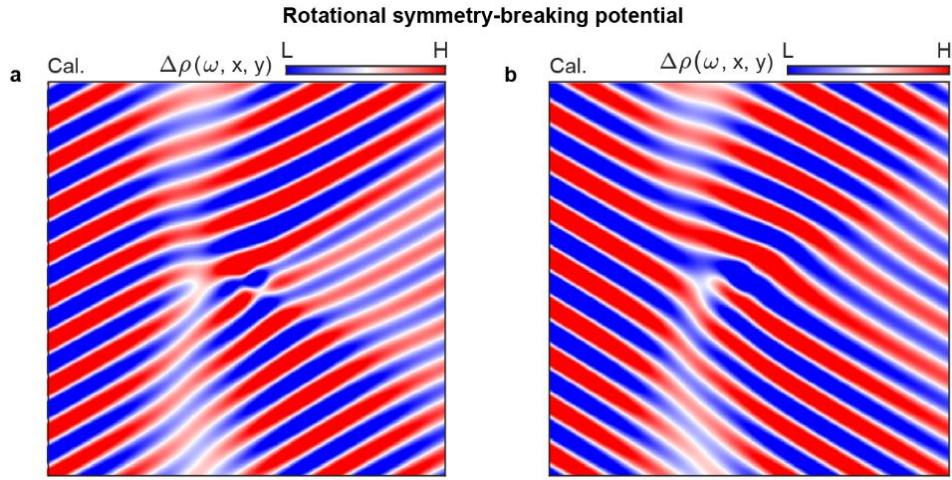
Extended Data Fig. 6 | Wavefront dislocations at different back-gate voltages. The sample bias 0.45 V and setpoint 0.2 A are consistent across all images. From the left to right panels, back-gate voltages are 2 V, 4 V, 6 V, and 8 V, respectively.



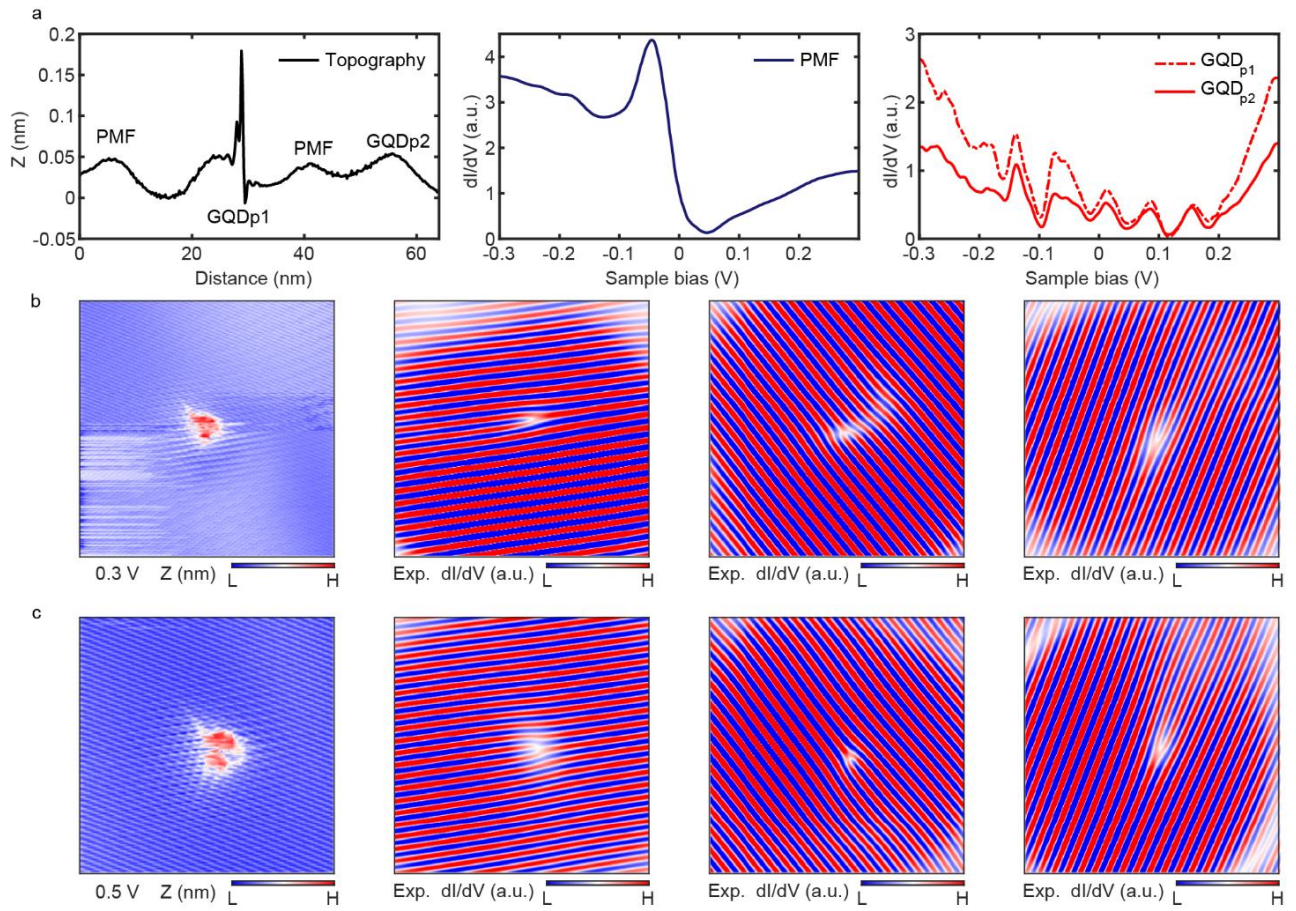
Extended Data Fig. 7 | The numerical results of dual-wavefront dislocations. **a**, The $\Delta\tilde{\rho}_A(\omega, r) \propto \text{Im}[\omega^2 H_0^2(\omega r) t(\omega)]$ and $\Delta\tilde{\rho}_B(\omega, r) \propto \text{Im}[\omega^2 H_1^2(\omega r) t(\omega)]$ for the energy of $\omega = 0.44$ eV. Here r has been converted to nm by multiplying the length unit $r^* = 10$ nm, and the dark circle denotes the first position for the emergence of additional wavefronts for the calculated result in Fig. 2e, where $\Delta\tilde{\rho}_A(\omega, r) = \Delta\tilde{\rho}_B(\omega, r)$. **b**, The numerically calculated distribution of $\Delta\rho(\omega, x, y)$ with $\omega = 0.15$ eV and $\Delta\vec{K} = \left(-\frac{4\pi}{3\sqrt{3}a_{cc}}, 0\right)$ under a rotationally symmetric Gaussian potential $V(r, \theta_r) = -V_0 e^{-\frac{r^2}{R^2}}$ with $V_0 \approx 0.25$ eV and $R = 18$ nm.



Extended Data Fig. 8 | The numerical results of the single wavefront dislocation for different energies. The numerically calculated distribution of $\Delta\rho(\omega, x, y)$ for different energies ω with $\Delta\vec{K} = \left(-\frac{4\pi}{3\sqrt{3}a_{cc}}, 0\right)$ under a potential $V(r, \theta_r) = -V_0 e^{-\frac{r^2}{R^2}} + V_1(r, \theta_r)$, which breaks the rotation symmetry similar to the calculated results in Fig. 2i. The single wavefront dislocation retains almost unchanged as ω varies. The energies are about 0.183 eV (panel **a**), 0.220 eV (panel **b**), and 0.292 eV (panel **c**).



Extended Data Fig. 9 | The numerically calculated distribution of $\Delta\rho(\omega, x, y)$ for different filtering directions. The energy is $\omega = 2$ (≈ 0.15 eV) under a potential $V(r, \theta_r) = -V_0 e^{-\frac{r^2}{R^2}} + V_1(r, \theta_r)$, which is similar as Extended Data Fig. 8a but for two distinct intervalley FFT-filtering directions. **a**, $\Delta\vec{K} = \left(\frac{2\pi}{3\sqrt{3}a_{cc}}, -\frac{2\pi}{3a_{cc}}\right)$. **b**, $\Delta\vec{K} = \left(\frac{2\pi}{3\sqrt{3}a_{cc}}, \frac{2\pi}{3a_{cc}}\right)$.



Extended Data Fig. 10 | Wavefront dislocations at different energies for the defect on the 1D strained substrate. **a**, Left panel: the height profile of the periodic strain structure. Middle panel: the strain-induced zeroth pseudo-Landau level spectrum. Right panel: pseudomagnetic confined states with an energy spacing of about 0.7 V. **b-c**, Single wavefront dislocation are observed at different energies, i.e., 0.3 V and 0.5 V, and different filtering directions.